value, and therefore unappreciable) is, however, accounted for by the model. The variability of the solar constant, and possible small changes in the thermo-optical coefficients due to ageing and temperature variations, are insignificant.

The question at what level can violations of general relativity be expected, does not have a satisfactory answer yet. A long-range scalar field is currently assumed to have a fundamental role in primordial cosmology: although it decays with the expansion of the Universe, its present remnant would entail not only violations of the two main tests of general relativity, but also a lack of universality of the constants of microphysics, as assumed in the equivalence principle[7,8]. A claim, based on quasar absorption lines, that the fine-structure constant α was weaker in the distant past has been made recently, thereby violating the equivalence principle[16–19]. If this claim is confirmed, and reconciled with other constraints on the variation of fundamental constants[20], such a finding would be the first serious challenge to Einstein's model. No detailed theory is available about the expected amounts of these violations, but $\gamma - 1$ should be negative and, possibly, in the range 10^{-5}–10^{-7}. Therefore, our result with accuracy not far from this range places an important constraint on this cosmological scenario. □

Method

The dynamical model used in the orbital fit is particularly simple, thanks to the large distance from the Sun, the location of the spacecraft in interplanetary space and the lack of unknown gravitational perturbations by Solar System bodies. The Jet Propulsion Laboratory's Orbit Determination Program has been used in the integration of the equations of motion and the orbital solution, based on planetary ephemerides and ancillary data, such as station location and Earth orientation parameters. To speed up the data processing, the observables have been compressed at $\tau = 300$ s by differencing the detected phases. Owing to the spectral characteristics of the noise (Supplementary Fig. S2), the data compression does not in any way affect the final result. We have used up to 12 free 'solve-for' parameters: (1) the six components of the state vector at the start of the experiment; (2) the three components of the non-gravitational acceleration due to the RTGs in the spacecraft frame; (3) the specular and diffuse reflectivity of the high-gain antenna, which determine the magnitude (and the direction) of the non-gravitational acceleration owing to solar radiation pressure; (4) the relativistic parameter γ. 'Consider' parameters (quantities not solved-for, but whose uncertainty is taken into account in the solution) include the dry troposphere, the station location, polar motion and the Earth Love numbers (which intervene in the solid tide model).

As discussed above, among the five parameters that control the non-gravitational acceleration, three (the non-radial components of the thermal thrust from the RTGs and one of the two optical coefficients of the high-gain antenna) are poorly determined. It is therefore appropriate to investigate a solution including only the other two, namely the radial acceleration due to the RTGs and the diffuse reflectivity of the antenna; by so doing, most non-gravitational perturbations are accounted for at a level consistent with the accuracy of the tracking data. The value of the other three parameters, the specular reflectivity and the non-radial components of the RTGs acceleration, together with their uncertainties have been taken from a separate fit carried out on the data from the Cassini solar opposition experiment, as mentioned above. This is our main orbital fit, with only nine parameters to be determined. The a priori uncertainty of the parameters that are not estimated, but affect the solution (such as the station geocentric coordinates and those derived from the gravitational wave experiment), has been included in the computation of the covariance matrix.

The data are assumed to be independent, but for each passage they are weighted with their own standard deviation. The variability of the results has been explored with different assumptions, in particular: a change in the threshold for discarding the outliers; different sampling time; and fitting separately the data before and after the conjunction. These trials clarified several issues including the structure of the covariance matrix, but did not in any way mar the final result.

The residuals of the orbital fit (Fig. 3) show a remarkably white spectrum (see Supplementary Fig. S2), which corresponds to the $\sim 1/\sqrt{\tau}$ observed dependence of both the root-mean-square (r.m.s.) deviation and the Allan deviation from the sampling time τ used in the orbital fit. After obvious outliers are removed (mostly introduced by incorrect tropospheric calibrations), the statistical distribution of the data shows a clearly gaussian behaviour.

We have also explored the full 12-parameter orbital fit and obtained similar results, with $\gamma = 1 + (1.35 \pm 2.47) \times 10^{-5}$, and no appreciable variation of the r.m.s. value of the residuals. Reassuringly, the non-gravitational accelerations so obtained are also fully consistent with the value obtained from the previous opposition experiment and with a long arc orbital solution generated by the Cassini Navigation Team using a data set spanning almost two years. In another trial, in addition to the spacecraft state vector we used just two free parameters—γ and a single, radial non-gravitational acceleration—and obtained the result $\gamma = 1 + (0.21 \pm 2.43) \times 10^{-5}$, with a small increase in the r.m.s. value of the residuals. The understanding of the physics involved and the number of different checks that have been performed have increased our confidence in the results.

Received 25 February; accepted 15 August 2003; doi:10.1038/nature01997.

1. Will, C. M. *Theory and Experiment in Gravitational Physics* (Cambridge Univ. Press, Cambridge, 1993).
2. Will, C. M. The confrontation between General Relativity and experiment. *Living Rev. Relativity* **4,** 4 (cited on 15 Aug 2003); at ⟨http://www.livingreviews.org/lrr-2001-4⟩.
3. Ciufolini, I. & Wheeler, J. A. *Gravitation and Inertia* (Princeton Univ. Press, Princeton, 1995).
4. Dyson, F. W., Eddington, A. S. & Davidson, C. A determination of the deflection of light by the Sun's gravitational field, from observations made at the total eclipse of May 29, 1919. *Phil. Trans. R. Soc. Lond. A* **220,** 291–333 (1920).
5. Lebach, D. E. *et al.* Measurement of the solar gravitational deflection of radio waves using very-long-baseline interferometry. *Phys. Rev. Lett.* **75,** 1439–1442 (1995).
6. Reasenberg, R. D. *et al.* Viking relativity experiment: verification of signal retardation by solar gravity. *Astrophys. J.* **234,** L219–L221 (1979).
7. Damour, T. & Polyakov, A. M. The string dilaton and a least coupling principle. *Nucl. Phys. B* **423,** 532–558 (1994).
8. Damour, T., Piazza, F. & Veneziano, G. Violations of the equivalence principle in a dilaton-runaway scenario. *Phys. Rev. D* **66,** 046007 (2002).
9. Iess, L., Giampieri, G., Anderson, J. D. & Bertotti, B. Doppler measurement of the solar gravitational deflection. *Class. Quant. Grav.* **16,** 1487–1502 (1999).
10. Bertotti, B. & Giampieri, G. Relativistic effects for Doppler measurements near solar conjunction. *Class. Quant. Grav.* **9,** 777–793 (1992).
11. Bertotti, B., Comoretto, G. & Iess, L. Doppler tracking of spacecraft with multifrequency links. *Astron. Astrophys.* **269,** 608–616 (1993).
12. Bertotti, B. & Giampieri, G. Solar coronal plasma in Doppler measurements. *Solar Phys.* **178,** 523–545 (1998).
13. Iess, L. *et al.* in *Aerospace Conf. Proc. (Montana, March 2003)* Vol. 1, 205–211 (Institute of Electrical and Electronics Engineers (IEEE), 2003).
14. Tortora, P., Iess, L. & Ekelund, J. E. in *Proc. World Space Congr. (Houston, 2002)* Paper IAC-02-Q.2.03 (AIAA, Reston, VA, 2002).
15. Tortora, P., Iess, L. & Herrera, R. G. in *Aerospace Conf. Proc. (Montana, March 2003)* Vol. 3, 1465–1473 (Institute of Electrical and Electronics Engineers (IEEE), 2003).
16. Murphy, M. T. *et al.* Possible evidence for a variable fine-structure constant from QSO absorption lines: motivations, analysis and results. *Mon. Not. R. Astron. Soc.* **327,** 1208–1222 (2001).
17. Murphy, M. T. *et al.* Possible evidence for a variable fine-structure constant from QSO absorption lines: systematic errors. *Mon. Not. R. Astron. Soc.* **327,** 1223–1236 (2001).
18. Murphy, M. T. *et al.* Further constraints on variation of the fine-structure constant from alkali-doublet QSO absorption lines. *Mon. Not. R. Astron. Soc.* **327,** 1237–1243 (2001).
19. Murphy, M. T. *et al.* Improved constraints on possible variations of physical constants from HI 21-cm and molecular QSO absorption lines. *Mon. Not. R. Astron. Soc.* **327,** 1244–1248 (2001).
20. Damour, T. String theory, cosmology and varying constants. *Astrophys. Space Sci.* **283,** 445–456 (2003).

Supplementary Information accompanies the paper on **www.nature.com/nature**.

Acknowledgements The work of B.B, L.I. and P.T. has been funded by the Italian Space Agency (ASI). The Jet Propulsion Laboratory Radio Science Systems Group, the engineers and staff of the DSS25 station, and the Cassini Project have been crucial for the success of this experiment. We thank J. W. Armstrong, J. J. Bordi and D. C. Roth for their contributions.

Competing interests statement The authors declare that they have no competing financial interests.

Correspondence and requests for materials should be addressed to L.I. (iess@hermes.ing.uniroma1.it).

Uniform resonant chaotic mixing in fluid flows

T. H. Solomon[1] **& Igor Mezić**[2]

[1]*Department of Physics, Bucknell University, Lewisburg, Pennsylvania 17837, USA*
[2]*Department of Mechanical and Environmental Engineering, University of California at Santa Barbara, Santa Barbara, California 93106, USA*

Laminar flows can produce particle trajectories that are chaotic[1,2], with nearby tracers separating exponentially in time. For time-periodic, two-dimensional flows and steady three-dimensional (3D) flows, enhancements in mixing due to chaotic advection are typically limited by impenetrable transport barriers that form at the boundaries between ordered and chaotic mixing regions. However, for time-dependent 3D flows, it has been proposed theoretically[3–5] that completely uniform mixing is possible through a resonant mechanism[5] called singularity-

induced diffusion; this is thought to be the case even if the time-dependent and 3D perturbations are infinitesimally small. It is important to establish the conditions for which uniform mixing is possible and whether or not those conditions are met in flows that typically occur in nature. Here we report experimental and numerical studies of mixing in a laminar vortex flow that is weakly 3D and weakly time-periodic. The system is an oscillating horizontal vortex chain (produced by a magnetohydrodynamic technique) with a weak vertical secondary flow that is forced spontaneously by Ekman pumping—a mechanism common in vortical flows with rigid boundaries, occurring in many geophysical, industrial and biophysical flows. We observe completely uniform mixing, as predicted[3–5] by singularity-induced diffusion, but only for oscillation periods close to typical circulation times.

Most previous studies of chaotic advection have focused on two-dimensional (2D), time-periodic flows. Transport barriers are prevalent in those flows[6]; in fact, chaotic transport barriers have been proposed as mechanisms for chemical isolation in geophysical flows[7,8], such as the Antarctic circumpolar region (the ozone hole) and Jupiter's Great Red Spot. Recent studies have further proposed that chaotic advection may have a pivotal role in the expanding field of microfluidic devices[9] and may also be important for many biophysical processes[10,11]. The possibility of chaotic motion of tracers in 3D flows was first suggested in 1966 (ref. 12) and was pursued numerically by another study[13]. However, systematic investigations of chaotic mixing in laminar 3D flows have only begun to appear in the literature during the past decade[3,4,14–24]. Further studies[3,4] extended the original work to show that uniform, barrier-free transport is possible through a mechanism called 'singularity-induced diffusion' (SID), even if the 3D and time-dependent perturbations are both infinitesimally small. A recent study[5] showed that a resonance mechanism is responsible for SID. When typical circulation frequencies are resonant with the driving frequency, saddle foci-type orbits enable tracers to spiral off one adiabatic surface and onto a different one, producing global mixing. An implication of this resonance picture, however, is that mixing will not be uniform if there are regions in the flow where the resonance condition is not met.

(Note that as SID—which applies to volume-preserving, time-dependent 3D flows—is enabled by spiral-node fixed points, it differs from another mechanism for global transport called 'Arnol'd diffusion', occurring in hamiltonian systems with more than 2 degrees of freedom.)

The flow studied here (Fig. 1) is dominated by a horizontal chain of alternating vortices with a secondary flow due to Ekman pump-

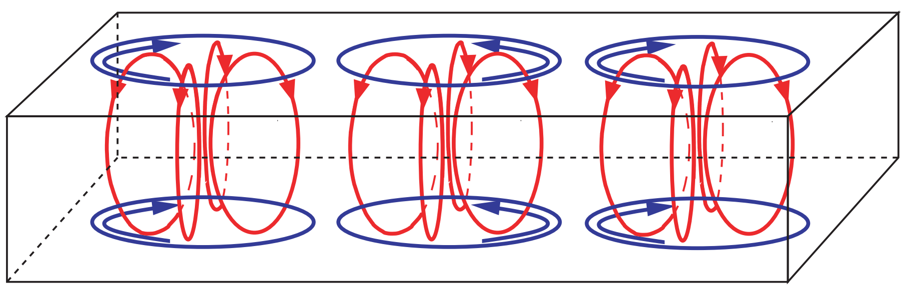

Figure 1 Sketch of a portion of the flow. The primary flow (blue) is a chain of alternating horizontal vortices; a weak secondary flow (red) is generated naturally by Ekman pumping, which draws fluid inward along the bottom of the vortices and up the vortex centres.

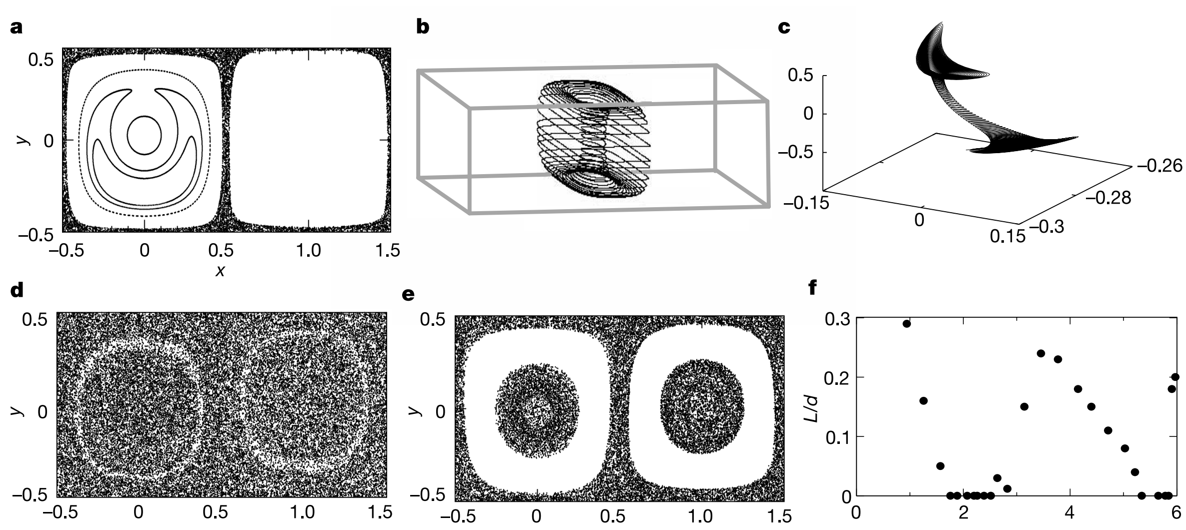

Figure 2 Numerical simulations of equations (1)–(3). **a**, Poincaré section for 2D, time-periodic case ($\epsilon = 0$, $b = 0.01$, $\omega = 2.5$), determined by plotting locations of five tracers once each period, initially located on the x axis at $x = 0.49$, 0.4, 0.3, 0.2 and 0.1. **b**, Trajectory of tracer in 3D, time-independent flow ($\epsilon = 0.005$, $b = 0$). **c**, Poincaré section for a tracer near a periodic orbit for 3D, time-periodic case ($\epsilon = 0.0001$, $b = 0.001$, $\omega = 2.5$), showing the tracer spiralling off one adiabatic surface (the spiral is very tightly wound and may be difficult to resolve) and onto a different one. **d**, Horizontal slice ($-0.1 < z < 0.1$) of Poincaré section of a single tracer for 3D, time-periodic case ($\epsilon = 0.005$, $b = 0.01$, $\omega = 2.5$); the tracer is initially located at $(x,y,z) = (0.49,0,0)$, and the forcing frequency is almost resonant with tracers circulating in the central torus. **e**, Horizontal slice of Poincaré section for a non-resonant forcing frequency ($\epsilon = 0.005$, $b = 0.01$, $\omega = 4.0$). **f**, Width L of the excluded region (as a fraction of the vortex width d) versus non-dimensional driving frequency ($\epsilon = 0.005$, $b = 0.01$). Uniform mixing is achieved for the frequencies where the width goes to zero.

ing, a process that occurs whenever a vortical flow is bounded by a solid surface. Radial pressure gradients due to the no-slip boundary condition push the fluid inward just above the solid boundary and up through the vortex centres. This is a common 3D flow perturbation; we therefore expect the internal mixing properties observed with this flow to be generic to a wide variety of vortical flows: basically, laminar vortex flows in the presence of a rigid boundary.

Time dependence takes the form of lateral oscillations of the vortex chain, similar to the oscillatory instability of Rayleigh–Bénard convection[25]. We have developed a model that captures the essential features of this flow:

$$v_x = \mathrm{d}x/\mathrm{d}t = -\cos(\pi x_s(t))\sin(\pi y) + \epsilon \sin(2\pi x_s(t))\sin(\pi z) \quad (1)$$

$$v_y = \mathrm{d}y/\mathrm{d}t = \sin(\pi x_s(t))\cos(\pi y) + \epsilon \sin(2\pi y)\sin(\pi z) \quad (2)$$

$$v_z = \mathrm{d}z/\mathrm{d}t = 2\epsilon \cos(\pi z)[\cos(2\pi x_s(t)) + \cos(2\pi y)] \quad (3)$$

Distances are scaled by the vortex width d, and time is scaled by the advective time d/U, where U is the maximum flow velocity. The lateral oscillation is accounted for by a shifted x-coordinate $x_s(t) = x + b\sin\omega t$, where b and ω are the non-dimensionalized oscillation amplitude and frequency. The strength of the secondary (3D) component of the flow is characterized by ϵ. This model is not intended to be a rigorous description of the flow in our experiments; rather, it is the simplest phenomenological model that captures the essential features of an alternating vortex flow with weak Ekman pumping. In particular, the model equations assume free-slip boundary conditions—a model with no-slip boundary conditions would have significantly more complicated y- and z-dependence[26,27]. Nevertheless, this simplified model successfully captures the dominant features of mixing in the experiments, as is shown below.

Numerical trajectories for the model are determined by integrating equations (1)–(3) using a fourth-order Runge–Kutta technique. The results are shown in Fig. 2. The 2D case ($\epsilon = 0$) is shown in Fig. 2a; trajectories are ordered in most of the flow, except for a chaotic band around and between the vortices. A tracer within the chaotic region never crosses into the ordered region in the vortex middle. A tracer trajectory for a 3D, time-independent flow is shown in Fig. 2b. An impurity near a vortex edge spirals upward, inward and then down through the centre and back out again. During this motion, the tracer visits different slices of the base 2D flow at different radii with different circulation times.

The mechanism for SID discussed in ref. 5 is seen numerically in Fig. 2c for a flow with weak time dependence and weak three-dimensionality. Near a resonance, a tracer spirals off what would have been an adiabatic surface (in the absence of SID) and onto a different surface. The result is nearly uniform mixing, as seen in Fig. 2d. But this mechanism works only if the frequency of oscillation is such that every tracer eventually reaches a radius with circulation frequency resonant with this driving frequency. Practically, this means that the oscillation frequency must be resonant with the circulation frequency for tracers in the lightened region in Fig. 2d. If forced at a different frequency, a toroidal region forms into and out of which there is zero or little mixing (Fig. 2e).

This resonant behaviour is plotted versus frequency in Fig. 2f; the frequencies where the width of the excluded region vanishes are those where uniform mixing should be expected. Practically, the frequency range for uniform mixing is slightly wider than shown in Fig. 2f, as molecular diffusion can mix impurities into the excluded region if the width is small. These results indicate a signature that should be seen in the experiments; namely, transport should be uniform or nearly uniform if forced at a frequency within or near these resonant bands, but should be characterized by toroidal regions of weak mixing if forced at different frequencies.

Experimentally, the flow in Fig. 1 is generated by a magneto-

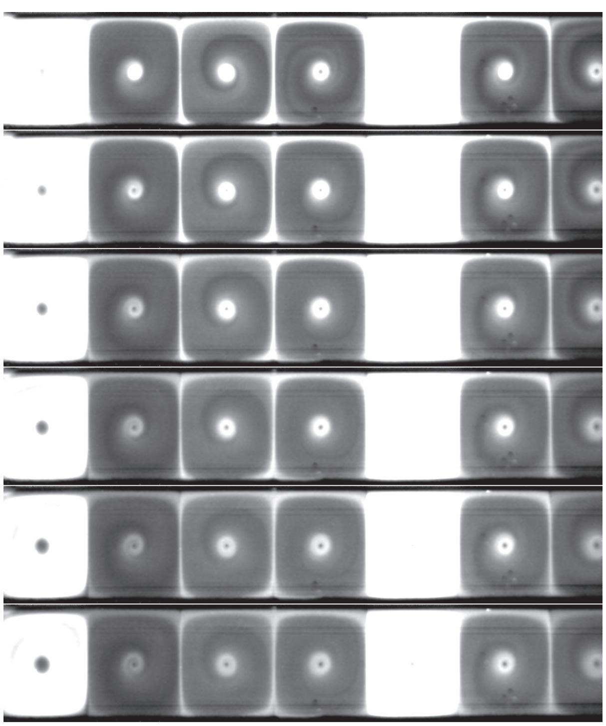

Figure 3 Experimental images of mixing for time-independent flow ($b = 0$). The same enhancement is used for all the images in this sequence. The images are saturated at large concentration values; consequently, decreases in the concentration of the injection vortices may not be noticeable in this figure or in Figs 4 and 5. For the time-independent case shown here, mixing is very slow both within and between the vortices. Concentration profiles for the centre vortex are available as Supplementary Information.

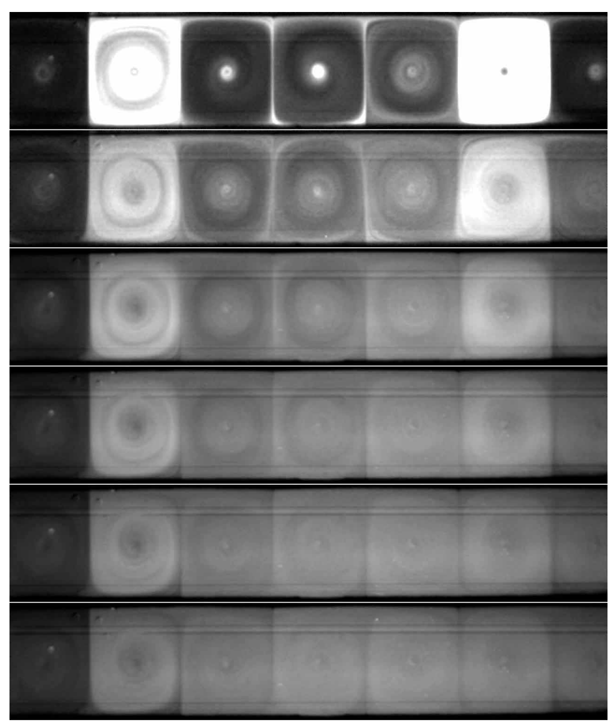

Figure 4 Experimental images of mixing for time-periodic flow forced near resonance ($b = 0.02$, 0.10 Hz oscillation frequency, corresponding to a non-dimensional angular frequency $\omega = 2.5$). The concentration becomes homogenized within the vortices. Concentration profiles for the centre vortex are available as Supplementary Information.

hydrodynamic technique[28,29] in which an electric current passes through a thin (2 mm) layer of dilute (0.006 M) H_2SO_4 with a free surface. The region of interest has horizontal dimensions 2.2×22 cm. The current interacts with an alternating magnetic field produced by magnets below the fluid; the result is a chain of vortices with a maximum velocity of approximately $7\,\mathrm{mm\,s^{-1}}$. Ekman pumping is generated spontaneously, owing to a glass plate below the vortices. For the impurity, we use fluorescent latex microspheres (0.103-μm diameter) with a diffusion coefficient 4.5×10^{-8} $\mathrm{cm^2\,s^{-1}}$, based on the Stokes–Einstein relation[30], small enough to minimize diffusive mixing. The flow is illuminated with black light, and the fluorescing microspheres are imaged by a CCD video camera.

When viewed from the side, the impurity can be seen moving inward slowly along the bottom and up through the centres of the vortices; from observations, it takes approximately ten horizontal circulation times (as measured for tracers circling in the outer portions of the vortices) for the impurity to circulate appreciably in the vertical direction owing to Ekman pumping. Images of mixing from above for a time-independent, 3D flow are shown in Fig. 3. In each experiment, we inject the impurity into two different vortices. During the injection process, some of the impurity slips out of these two vortices and into the edges of the neighbouring vortices. Left undisturbed (and with no time dependence) for 20 min, Ekman pumping carries some of the impurity into the centres of the vortices. The result is the '$t = 0$ min' case in which most vortices have a thin line of impurity around the edges and spots in the centre. For Fig. 3, we leave the system undisturbed after this initial condition. The result for this time-independent case is very slow internal mixing.

Figure 4 shows mixing for the case with weak time-periodic forcing with a frequency resonant with the typical circulation frequencies. Within about 25 min (approximately 150 oscillation periods), the impurity concentration is almost completely uniform within the vortices. The mixing is different in a subtle but important way if the frequency of the time dependence is in a non-resonant band (Fig. 5). There is still significant mixing within the vortices. However, there are toroidal regions into which impurity does not mix readily: these regions appear in Fig. 5 as darkened annuli, and they persist for over an hour. These darkened annuli are the excluded toroidal regions seen in the simulations (compare Fig. 5 with Fig. 2e).

For the run shown in Fig. 5, mixing of the impurity out of the two injection vortices is also retarded by the transport barriers. For later times (not shown), higher concentrations persist in the tori in these two vortices; in fact, a brightened torus is still clear after 2 h in the left-most vortex. At this point, we change the oscillation frequency back to the original resonant value, and the brightened region quickly dissipates (in 5–10 min), further evidence of the resonant nature of this internal mixing. (See Supplementary Information for a video of this, along with videos of the sequences of Figs 4 and 5.)

We find that mixing in a weakly 3D, weakly time-periodic flow is nearly uniform, but only if forced at a period resonant with the typical circulation times; specifically, circulation times at radii corresponding to the centres of what would otherwise be the excluded tori. This restriction might seem to limit the applicability of SID as a mechanism for uniform mixing in real flows; however, in nature, flows often choose precisely this circulation frequency for time-periodic instabilities. In fact, in the experiments presented here, it is experimentally challenging to avoid internal mixing because even very slight time-dependent perturbations due to aggregation of the latex microspheres or due to any advected floating scum in the system results in significantly enhanced internal mixing. Both of these mechanisms result in time dependence with frequencies determined by circulation frequencies, so the resonant condition is satisfied automatically. As time-dependent perturbations are often linked to circulation, we expect uniform mixing to be common in many natural vortex flows with Ekman pumping. □

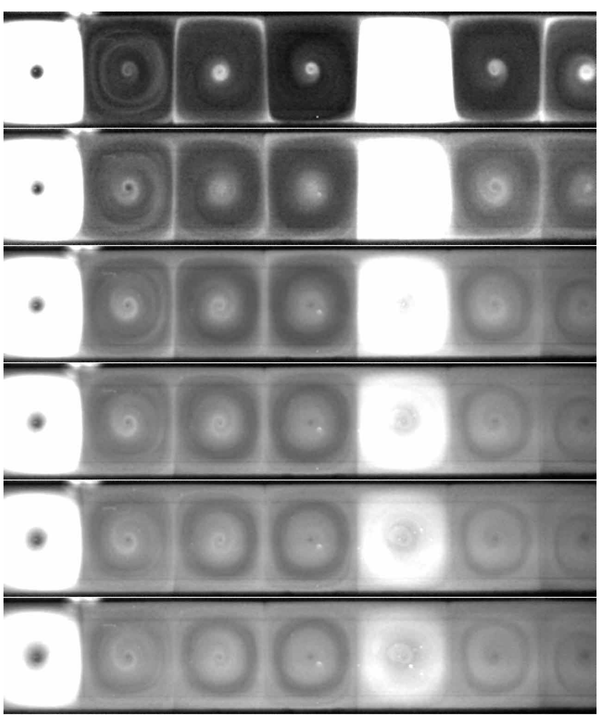

Figure 5 Experimental images of mixing for time-periodic flow forced away from a resonant band ($b = 0.02$, 0.160 Hz oscillation frequency, corresponding to a non-dimensional angular frequency $\omega = 4.2$). Darkened annular bands are seen in the later images, indicating regions into which mixing is weak. Concentration profiles for the centre vortex are available as Supplementary Information.

Received 30 June; accepted 11 August 2003; doi:10.1038/nature01993.

1. Aref, H. Stirring by chaotic advection. *J. Fluid Mech.* **143,** 1–21 (1984).
2. Aref, H. Fluid dynamics: Order in chaos. *Nature* **401,** 756–758 (1999).
3. Feingold, M., Kadanoff, L. P. & Piro, O. Passive scalars, 3-dimensional volume-preserving maps and chaos. *J. Stat. Phys.* **50,** 529–565 (1988).
4. Cartwright, J. H. E., Feingold, M. & Piro, O. Chaotic advection in three-dimensional unsteady incompressible laminar flow. *J. Fluid Mech.* **316,** 259–284 (1996).
5. Mezić, I. Break-up of invariant surfaces in action-angle-angle maps and flows. *Physica D* **154,** 51–67 (2001).
6. Rom-Kedar, V., Leonard, A. & Wiggins, S. An analytical study of transport, mixing and chaos in an unsteady vortical flow. *J. Fluid Mech.* **214,** 347–394 (1990).
7. Behringer, R. P., Meyers, S. D. & Swinney, H. L. Chaos and mixing in a geostrophic flow. *Phys. Fluids A* **3,** 1243–1249 (1991).
8. Pierrehumbert, R. T. Large scale horizontal mixing in planetary atmospheres. *Phys. Fluids A* **3,** 1250–1260 (1991).
9. Stroock, A. D., Dertinger, S. K. W., Mezić, I., Stone, H. A. & Whitesides, G. M. Chaotic mixer for microchannels. *Science* **295,** 647–651 (2002).
10. Karolyi, G., Pentek, A., Scheuring, I., Tel, T. & Toroczkai, Z. Chaotic flow: The physics of species coexistence. *Proc. Natl Acad. Sci. USA* **25,** 13661–13665 (2000).
11. Swanson, P. D., Muzzio, F. J., Annapragada, A. & Adjei, A. Numerical analysis of motion and deposition of particles in cascade impactors. *Int. J. Pharm.* **142,** 33–51 (1996).
12. Arnold, V. I. Sur la geometrie differentielle des groupes de lie de dimension infinie et ses applications I l'hydrodynamique des fluides parfaits. *Ann. Inst. Fourier* **16,** 316–361 (1966).
13. Hénon, M. Sur la topologie des lignes de courant dans un cas particulier. *C. R. Acad. Sci. Paris A* **262,** 312–314 (1966).
14. Bajer, K. & Moffatt, H. K. On a class of steady confined Stokes flows with chaotic streamlines. *J. Fluid Mech.* **212,** 337–363 (1990).
15. Stone, H. A., Nadim, A. & Strogatz, S. H. Chaotic streaklines inside drops immersed in steady linear flows. *J. Fluid Mech.* **232,** 629–646 (1991).
16. Holm, D. D. & Kimura, Y. Zero-helicity Lagrangian kinematics of three dimensional advection. *Phys. Fluids A* **3,** 1033–1038 (1991).
17. Mackay, R. S. Transport in 3-D volume-preserving flows. *J. Nonlinear Sci.* **4,** 329–354 (1994).
18. Mezić, I. & Wiggins, S. On the integrability and perturbation of three dimensional fluid flows with symmetry. *J. Nonlinear Sci.* **4,** 157–194 (1994).
19. Ashwin, P. & King, G. P. Streamline topology in eccentric Taylor vortex flow. *J. Fluid Mech.* **285,** 215–247 (1995).
20. Fountain, G. O., Khakhar, D. V., Mezić, I. & Ottino, J. M. Chaotic mixing in a bounded 3D flow. *J. Fluid Mech.* **417,** 265–301 (2000).
21. Sotiropoulos, F., Ventikos, Y. & Lackey, T. C. Chaotic advection in 3-D stationary vortex-breakdown bubbles: Šil'nikov's chaos and the devil's staircase. *J. Fluid Mech.* **444,** 257–297 (2001).

22. Fountain, G. O., Khakhar, D. V. & Ottino, J. M. Visualization of three-dimensional chaos. *Science* **281,** 683–686 (1998).
23. Shinbrot, T., Alvarez, M. M., Zalc, J. M. & Muzzio, F. J. Attraction of minute particles to invariant regions of volume preserving flows by transients. *Phys. Rev. Lett.* **86,** 1207–1210 (2001).
24. Vainshtein, D. L., Vasiliev, A. A. & Neishtadt, A. J. Changes in the adiabatic invariant and streamline chaos in confined incompressible Strokes flow. *Chaos* **6,** 67–77 (1996).
25. Clever, R. M. & Busse, F. H. Transition to time-dependent convection. *J. Fluid Mech.* **65,** 625–645 (1974).
26. Solomon, T. H. & Gollub, J. P. Chaotic particle transport in time-dependent Rayleigh-Bénard convection. *Phys. Rev. A.* **38,** 6280–6286 (1988).
27. Chandresekhar, S. *Hydrodynamic and Hydromagnetic Stability* 39 (Clarendon, Oxford, 1961).
28. Solomon, T. H., Tomas, S. & Warner, J. L. The role of lobes in chaotic mixing of miscible and immiscible impurities. *Phys. Rev. Lett.* **77,** 2682–2685 (1996).
29. Solomon, T. H., Tomas, S. & Warner, J. L. Chaotic mixing of immiscible and immiscible impurities in a two-dimensional flow. *Phys. Fluids* **10,** 342–350 (1998).
30. Cussler, E. L. *Diffusion: Mass Transfer in Fluid Systems* (Cambridge Univ. Press, Cambridge, 1984).

Supplementary Information accompanies the paper on **www.nature.com/nature**.

Acknowledgements This work was supported by the US National Science Foundation, AFOSR, and by a Sloan Fellowship grant.

Competing interests statement The authors declare that they have no competing financial interests.

Correspondence and requests for materials should be addressed to T.S. (tsolomon@bucknell.edu) or I.M. (mezic@engineering.ucsb.edu).

Microwave oscillations of a nanomagnet driven by a spin-polarized current

S. I. Kiselev[1]*, J. C. Sankey[1]*, I. N. Krivorotov[1], N. C. Emley[1], R. J. Schoelkopf[2], R. A. Buhrman[1] & D. C. Ralph[1]

[1]*Cornell University, Ithaca, New York 14853, USA*
[2]*Department of Applied Physics and Physics, Yale University, New Haven, Connecticut 06511, USA*

* These authors contributed equally to this work

The recent discovery that a spin-polarized electrical current can apply a large torque to a ferromagnet, through direct transfer of spin angular momentum, offers the possibility of manipulating magnetic-device elements without applying cumbersome magnetic fields[1–16]. However, a central question remains unresolved: what type of magnetic motions can be generated by this torque? Theory predicts that spin transfer may be able to drive a nanomagnet into types of oscillatory magnetic modes not attainable with magnetic fields alone[1–3], but existing measurement techniques have provided only indirect evidence for dynamical states[4,6–8,12,14–16]. The nature of the possible motions has not been determined. Here we demonstrate a technique that allows direct electrical measurements of microwave-frequency dynamics in individual nanomagnets, propelled by a d.c. spin-polarized current. We show that spin transfer can produce several different types of magnetic excitation. Although there is no mechanical motion, a simple magnetic-multilayer structure acts like a nanoscale motor; it converts energy from a d.c. electrical current into high-frequency magnetic rotations that might be applied in new devices including microwave sources and resonators.

We examine samples made by sputtering a multilayer of composition 80 nm Cu/40 nm Co/10 nm Cu/3 nm Co/2 nm Cu/30 nm Pt onto an oxidized silicon wafer and then milling through part of the multilayer (Fig. 1a) to form a pillar with an elliptical cross-section of lithographic dimensions 130 nm × 70 nm (ref. 17). Top contact is made with a Cu electrode. Transmission or reflection of electrons from the thicker 'fixed' Co layer produces a spin-polarized current that can apply a torque to the thinner 'free' Co layer. Subsequent oscillations of the free-layer magnetization relative to the fixed layer change the device resistance[18] so, under conditions of d.c. current bias, magnetic dynamics produce a time-varying voltage (with typical frequencies in the microwave range). If the oscillations were exactly symmetric relative to the direction of the fixed-layer moment, voltage signals would occur only at multiples of twice the fundamental oscillation frequency, f. To produce signal strength at f, we apply static magnetic fields (H) in the sample plane a few degrees away from the magnetically easy axis of the free layer. All data are taken at room temperature, and by convention positive current I denotes electron flow from the free to the fixed layer.

In characterization measurements done at frequencies <1 kHz, the samples exhibit the same spin-transfer-driven changes in resistance reported in previous experiments[7,9] (Fig. 1b). For H smaller than the coercive field of the free layer ($H_c \approx 600$ Oe), an applied current produces hysteretic switching of the magnetic layers between the low-resistance parallel (P) and high-resistance anti-parallel (AP) states. Sweeping H can also drive switching between the P and AP states (Fig. 1b, inset). For H larger than 600 Oe, the current produces peaks in the differential resistance dV/dI that have been assumed previously to be associated with dynamical magnetic excitations[4,6–8]. The resistance values displayed in Fig. 1b include a lead resistance of ~6 Ω from high-frequency (50 GHz) probes and a top-contact resistance of ~9 Ω.

We measure the spectra of microwave power that result from magnetic motions by using a heterodyne mixer circuit[19] (Fig. 1a). This circuit differs from the only previous experiment to probe spin-transfer-driven magnetic oscillations[8] in that the sample is not exposed to a large high-frequency magnetic field that would alter its dynamics. The filter on the output of our mixer passes 25–100 MHz, giving a frequency resolution of ~200 MHz. We calibrate the circuit by measuring temperature-dependent Johnson noise from test resistors. When we state values of emitted power, they will correspond to the power available to a load matched to the sample resistance, R. To convert to the power delivered to a 50-Ω line, one should divide our values by the power transmission coefficient $1 - \Gamma^2 = 1 - [(R - 50\ \Omega)/(R + 50\ \Omega)]^2$.

We first consider the microwave spectrum from sample 1 for $H = 2$ kOe. For both negative I and small positive I we measure only frequency-independent Johnson noise. We will subtract this background from all the spectra we display. At $I = 2.0$ mA, we begin to resolve a microwave signal at 16.0 GHz (Fig. 1c, d). A second-harmonic peak is also present (Fig. 1c, inset). As I is increased, these initial signals grow until $I \approx 2.4$ mA, beyond which the dynamics change to a different regime (Fig. 1d). In Fig. 1e, we compare the H-dependence of the measured frequency for the initial signals to the formula for small-angle elliptical precession of a thin-film ferromagnet[20]:

$$f = \frac{\gamma}{2\pi}\sqrt{(H + H_{\mathrm{an}} + H_d)(H + H_{\mathrm{an}} + H_d + 4\pi M_{\mathrm{eff}})} \qquad (1)$$

Here γ is the gyromagnetic ratio, H_{an} accounts for a uniaxial easy-axis anisotropy, H_{d} models the coupling from the fixed layer, and $4\pi M_{\mathrm{eff}} = 4\pi M_{\mathrm{s}} - 2K_{\mathrm{u}}/M_{\mathrm{s}}$, with M_{s} the saturation magnetization and K_{u} a uniaxial perpendicular anisotropy[21]. The fit is excellent and gives the values $4\pi M_{\mathrm{eff}} = 6.8 \pm 0.1$ kOe and $H_{\mathrm{an}} + H_{\mathrm{d}} = 1.18 \pm 0.04$ kOe. The value for $4\pi M_{\mathrm{eff}}$ is less than $4\pi M_{\mathrm{s}}$ for bulk Co (16 kOe) as expected due to significant perpendicular anisotropy in Co/Cu(111) films (see Fig. 3 in ref. 22). Similar fits for other samples yield $4\pi M_{\mathrm{eff}}$ in the range 6.7–12 kOe. Superconducting quantum interference device (SQUID) measurements on test samples containing many 3-nm Co layers give $4\pi M_{\mathrm{eff}} = 10 \pm 1$ kOe.